Loss of *cped1* does not affect bone and lean mass in zebrafish

Short Title

Role of *cped1* in zebrafish musculoskeletal tissues

Kurtis Alvarado[1,2¶], W. Joyce Tang[1,2¶], Claire J. Watson[1,2], Ali R. Ahmed[1,2], Arianna Ericka Gomez[1,2], Rajashekar Donaka[3], Chris Amemiya[5], David Karasik[3,4], Yi-Hsiang Hsu[4], Ronald Young Kwon[1,2*]

[1] Department of Orthopaedic Surgery and Sports Medicine, University of Washington School of Medicine, Seattle, WA, USA

[2] Institute for Stem Cell and Regenerative Medicine, University of Washington, Seattle, WA, USA

[3] The Azrieli Faculty of Medicine, Bar-Ilan University, Safed, Israel

[4] Hebrew SeniorLife, Hinda and Arthur Marcus Institute for Aging Research, Boston, MA, USA

[5] Department of Molecular and Cell Biology and Quantitative and Systems Biology Program, University of California, Merced, CA, USA.

* Corresponding author

E-mail: ronkwon@uw.edu

¶These authors contributed equally to this work.

Abstract

Human genetic studies have nominated Cadherin-like and PC-esterase Domain-containing 1 (*CPED1*) as a candidate target gene mediating bone mineral density (BMD) and fracture risk heritability. Recent efforts to define the role of *CPED1* in bone in mouse and human models have revealed complex alternative splicing and inconsistent results arising from gene targeting, making its function difficult to interpret. To better understand the role of *CPED1* in adult bone mass and morphology, we turned to zebrafish, an emerging model for orthopaedic research. We analyzed two different *cped1* mutant lines and performed deep phenotyping to characterize more than 200 measures of adult vertebral, craniofacial, and lean tissue morphology. We also examined alternative splicing of zebrafish *cped1* and gene expression in various cell/tissue types. Our studies fail to support an essential role of *cped1* in adult zebrafish bone. Specifically, homozygous mutants for both *cped1* mutant alleles, which are expected to result in loss-of-function and impact all *cped1* isoforms, exhibited no significant differences in the measures examined when compared to their respective wildtype controls, suggesting that *cped1* does not significantly contribute to these traits. We identified sequence differences in critical residues of the catalytic triad between the zebrafish and mouse orthologs of CPED1, and discuss how these differences, as well as distinct alternative splicing, could underlie different functions of *CPED1* orthologs in the two species. Our studies demonstrate that *cped1* is not required for normal adult zebrafish bone mass, lean mass, or bone and lean mass morphology, adding to evidence that variants at 7q31.31 can act independently of *CPED1* to influence BMD and fracture risk.

Introduction

Understanding genetic risk for osteoporosis is important to reduce this massive health burden. It has been estimated that up to 89% of the variation in bone mineral density (BMD), a key indicator for diagnosing osteoporosis and predicting fracture risk, is determined by genetics [1]. Over the past several decades, a large number of human genetic studies have nominated Cadherin-like and PC-esterase Domain-containing 1 (*CPED1*) as a candidate target gene mediating BMD and fracture risk heritability. In particular, genome-wide association studies (GWAS) have identified human chromosome region 7q31.31, also known as the *CPED1-WNT16* locus, to be associated with BMD and fracture [2-9]. Of the five genes at this locus (*WNT16*, *CPED1*, *ING3*, *FAM3C*, and *TSPAN12*), *WNT16* is the most studied and characterized [10]. *In vivo* mouse studies have shown that *Wnt16* is necessary for bone mass and strength [5, 6], in part by suppressing osteoclastogenesis [11] and promoting osteoblastogenesis [12] in cortical bone. Moreover, functional studies in zebrafish have found that *wnt16* is an important regulator of bone formation, fracture susceptibility, and morphogenesis [13-15], further supporting the hypothesis that *wnt16* is a causal gene at this locus. Intriguingly, in the GWAS by Medina-Gomez et al., two independent signals were identified at this locus, with the second signal mapping to the intronic region of *CPED1* [5]. These two signals were significant even after accounting for genetic linkage. It has been postulated that the presence of multiple independent signals at the *CPED1-WNT16* locus could reflect several causal variants that act on distinct genes [5, 10]. Recently, Chesi et al. performed high-resolution Capture C combined with ATAC-seq and found significant interactions between the *CPED1* promoter and SNPs which served as proxies for the BMD sentinel SNP [16], evidence of the potential for *CPED1* to function as a target gene at the *CPED1-WNT16* locus, possibly in tandem with *WNT16* [10].

The biological function of the encoded protein for *CPED1* is poorly characterized. Previously known as *C7orf58*, *CPED1* was identified in a search for homologs of *Cas1p*, which encodes a fungal protein that has a novel N-terminal globular domain predicted to interact with and modify glycoproteins at the cell surface [17]. Named the PC-esterase domain, proteins possessing this feature are found exclusively in the eukaryotic kingdom [18]. Metazoan members of the PC-esterase family were found to have three additional predicted domains fused to the N-terminus of the PC-esterase domain: a signaling peptide sequence to target the protein to the secretory pathway at the plasma membrane, a domain related to the tubulin-tyrosine ligase family, and a cadherin-like domain predicted to form a beta-sandwich structure that allows for extracellular interactions such as carbohydrate binding.

Recent efforts have sought to define the role of *CPED1* in bone. Medina-Gomez et al. first explored the role of *CPED1* in bone by assessing the relationship between *CPED1* expression and BMD. These authors found that high *CPED1* expression is associated with lower BMD, as evidenced by a strong inverse correlation between *CPED1* transcript levels in human iliac crest samples and total body BMD and skull BMD [5]. Subsequently, Maynard et al. performed the first in-depth experimental characterization of *Cped1* transcription and identified *Cped1* transcripts in multiple mouse tissues including bone [1]. Interestingly, in addition to identifying full-length transcripts, they observed multiple alternatively spliced isoforms with missing exons, including in-frame exon deletions, as well as a severely truncated transcript predicted to encode proteins missing the cadherin-like and PC-esterase domains. They also identified several alternative transcription start sites predicted to encode for proteins with N-terminal truncations. Several functional studies examining the consequences of targeted *CPED1* knockdown have also been conducted. Chesi et al. performed siRNA-knockdown of *CPED1* in primary human MSCs subjected to osteogenic differentiation [16]. These authors found that *CPED1* knockdown by targeting multiple exons did not consistently alter BMP2-induced osteoblastic differentiation, suggesting that *CPED1* may not be required for osteoblastic differentiation in human MSCs. In contrast, in a recent conference abstract, it was reported that in MC3T3-L1 mouse pre-osteoblastic cells, *Cped1* knockdown by siRNAs reduced or enhanced osteoblast differentiation, depending on the targeted exon, presumably due to differential targeting of different transcript isoforms [19]. In a separate conference abstract, it was reported that male mice homozygous for a CRISPR/Cas9-induced nonsense mutation in *Cped1* exhibited reduced femoral strength compared to wildtype controls as assessed by three-point flexion [20]. In summary, functional studies in mouse and *in vitro* human models have produced variable results following targeted knockdown of *CPED1*.

This variability, in concert with the complex splicing of *CPED1*, make its role in bone difficult to interpret. Thus, further studies examining the function of *CPED1* in bone are needed.

To better understand the role of *CPED1* in adult bone mass and morphology, we took advantage of the zebrafish system. Zebrafish are an emerging model for orthopaedic research due in part to their ease of genetic manipulation and amenability to deep skeletal phenotyping at the whole-body scale, enabling efficient testing of candidate genes nominated by GWAS [21-24]. We analyzed two different *cped1* mutant lines and performed deep phenotyping to characterize more than 200 measures of adult vertebral, craniofacial, and lean tissue morphology. We also examined alternative splicing of zebrafish *cped1* and gene expression in various cell/tissue types. Our studies fail to support an essential role of *cped1* in adult zebrafish bone. Specifically, homozygous mutants for both of the analyzed *cped1* alleles, which are expected to result in loss-of-function and impact all *cped1* isoforms, exhibited no significant differences in the measures examined when compared to their respective wildtype controls, suggesting that *cped1* does not significantly contribute to these traits. We identified sequence differences in critical residues of the catalytic triad between the zebrafish and mouse orthologs of CPED1, and discuss how these differences, as well as distinct alternative splicing, could underlie different functions of *CPED1* orthologs in the two species. Lastly, we discuss how our studies support evidence from the literature that variants at 7q31.31 can act independently of *CPED1* to influence BMD and fracture risk.

Materials and Methods

Ethics statement

All studies were performed on an approved protocol in accordance with the University of Washington Institutional Animal Care and Use Committee (IACUC).

Animal care

Zebrafish were housed at 28.5°C following a 14:10 hour light:dark cycle, and provided with a standard commercial diet. Research was carried out using mixed sex wildtype (AB) and two *cped1* mutant lines (*cped1*^{sa20221}, *cped1*^{w1003}). The *cped1*^{sa20221} line, which has a single nucleotide variant in exon 15, was purchased from the Zebrafish International Resource Center (Eugene, OR). We used the following primers for genotyping *cped1*^{sa20221}: F: 5' – GCCCCTGTGCAAAGTGTTAAG – 3', R: 5' – CACAGAAAGAAAAATGGGCGGT – 3'. PCR was performed using standard conditions (35 cycles, annealing temperature of 58°C) [15], and products were run on high-resolution 3% agarose gels. Sanger sequencing was used to identify *cped1*^{sa20221} mutant PCR products. *cped1*^{w1003} mutants were previously described in Watson et al. [15]. MicroCT scans of 90 days post fertilization (dpf) *cped1*^{w1003} mutants and wildtype clutchmates generated in the study of Watson et al. were reanalyzed for this study; no new experiments in *cped1*^{w1003} mutants were performed.

RT-PCR and tissue-specific *cped1* expression

Total RNA was harvested from adult AB wildtype and homozygous mutant fish using homogenization in TRIzol (Invitrogen), adhering to the protocol specified by the manufacturer. To analyze *cped1* transcript expression in different zebrafish organs, two adult male and two adult female wildtype fish were euthanized in an ice bath and dissected using the methods described by Gupta et al [25]. Organs were harvested and preserved in RNALater at -80°C until RNA isolation was performed. Total RNA was collected from vertebral bone, skeletal muscle, intestine, whole brain, skin, swim bladder, heart, eyes, and testes. cDNA synthesis was performed with the Superscript IV First Strand Synthesis System (ThermoFisher) and 1 uL of each cDNA was used for PCR amplification. All products were electrophoresed on a single 3% agarose gel, and bands of interest were excised from the gel for DNA extraction followed by Sanger sequencing to validate the yielded product. To test for the effects of the *cped1*^{sa20221} mutation on transcript expression and splicing, we used the following primers targeting exons 14 and 16 to flank the SNP mutation in exon 15: F: 5'–GCAGAATCAACATTCTGGTGATGGA–3', R: 5'–CAGGACTGCAGCTGAGGTTGAT–3'.

Single-cell RNA-seq analysis

We obtained the zebrafish embryonic single-cell RNA-seq (scRNA-seq) dataset by Saunders et al. [26] from the NCBI Gene Expression Omnibus repository (GSE202639). All analyses were performed using Monocle (v3) and Seurat (v4) in R [27-29]. Average expression values were determined using the AverageExpression() function, which exponentiates the log normalized count data prior to calculating the average value.

microCT scanning and analysis

Fish were scanned at 90 dpf using a vivaCT40 microCT scanner (Scanco Medical, Switzerland) with the following parameters: 21 µm voxel resolution, 55kVp, 145mA, 1024 samples, 500proj/180°, 200 ms integration time [30, 31]. Scanco software was used to generate DICOM files for each fish, and subsequent analyses were performed on maximum intensity projections of the DICOM images. Four fish were scanned simultaneously in each acquisition. Vertebral bone analysis was performed using FishCuT, as outlined in [31, 32].

To calculate lean tissue volume, we followed the procedures described in Watson et al [15]. Briefly, DICOM files were opened in Fiji [33] and a single slice from the midpoint of the stack, adjacent to the posterior swim bladder, was chosen for analysis. Lower and upper thresholds were automatically determined using the Default and MaxEntropy threshold algorithms within Fiji. Subsequently, a custom MATLAB script was used to open DICOM files and perform voxel segmentation based on intensity into three tissue compartments: presumptive adipose (below lower threshold), lean (between lower and upper threshold), and bone (above upper threshold).

Craniofacial analysis

To examine craniofacial shape variation, we employed landmarking methods we have previously described [34, 35]. Thirteen landmarks (S1 Table), which were derived from Diamond et al. 2022 [34], were manually placed on anatomical prominences of the zebrafish skull using the markups module in 3DSlicer (www.slicer.org) [36]. The distance between specific pairs of points was calculated, providing a total of seven measurements: skull length (from the most anterior point of the frontal bone to the most dorsal part of the first vertebrae), frontal bone length, epiphyseal bar length, distance between anguloarticulars, dorsal skull width (distance between pterotic cartilage bones), midline skull width (distance between the most posterior part of opercles), and ventral skull width (distance between the sutures connecting the opercle and interopercle). We chose these measurements based on past studies showing morphological alterations of the opercular region and frontal and parietal bones in response to mutations in genes associated with human skeletal conditions [34, 35]. For analysis, we normalized the measurements for each fish based on its standard length and performed a t-test for each measurement using the statistical analysis software, Prism (v8, GraphPad). We excluded fish exhibiting gross deformations to the skull arising from sample processing for microCT scanning, leaving 6 homozygous *cped1*^{w1003} mutants, 7 homozygous *cped1*^{sa20221} mutants, as well as 7 of each of their respective wildtype clutchmates.

Multiple sequence alignment

All amino acid sequences for the multiple sequence alignment were obtained from the NCBI protein database, using the isoforms with the longest annotated sequences. The sequences were aligned with the MUSCLE alignment software (version 3.8.425) on the EMBL-EBI website. We used the ggmsa package (v1.0.3) in R to determine the consensus sequence and to plot the alignment [37].

Statistical approach

For most results, data are reported from a single experiment. Each biological replicate represents one technical replicate. Empirical data are shown as either individual measurements or are reported as mean ± SEM. Group sizes (n) are reported in the figure panels themselves or in respective legends. Outliers

were not identified; all data were included in statistical analyses. Multivariate analysis of vertebral data using the global test was performed using the globaltest package in R [31]. All other statistical analyses were performed in GraphPad Prism as described in the text. $p<0.05$ was considered statistically significant in all cases.

Results and Discussion

Alternative splicing of *CPED1* orthologs is species-dependent

The zebrafish *cped1* gene is located on chromosome 4 and exhibits synteny with the human *CPED1-WNT16* locus, with *cped1* flanked on the 5' end by *ing3* and on the 3' end by *wnt16*. Two alternatively spliced transcripts are annotated in the zebrafish GRCz11 (GCA_000002035.4) genome assembly on ENSEMBL, *cped1*-201 and *cped1*-202 (ENSDART00000067251.6 and ENSDART00000143690.4, respectively) (Fig 1A, top). Both transcripts contain 21 exons, with exons 1, 11, 12, 13, 17, 18, 19, and 21 exhibiting differences at the 5' or 3' end of the exon likely due to alternative donor and acceptor sites. Notably, whereas transcript isoforms exhibiting exon skipping are annotated for mouse *Cped1* [1], no such isoforms were annotated for zebrafish *cped1*.

To examine alternative splice events in zebrafish *cped1*, we analyzed several public databases. First, to characterize such events in zebrafish embryos and larvae, we queried the MeDAS database, which utilizes public RNA-seq data to characterize alternative splicing events in developmental time course experiments. MeDAS quantifies inclusion of exons as well as exonic regions that contribute to different 5' or 3' boundaries [38]. Our query identified three alternative splicing events in zebrafish *cped1* that were detected by the MeDAS pipeline, consisting of alternative exon boundary regions at the 3' end of exon 12, the 3' end of exon 17, and the 5' end of exon 19 (Fig 1A, bottom). None of these alternative splice events showed significant differences in expression across developmental stages (Kruskal-Wallis $p>0.05$ for all three events, as determined by the MeDAS pipeline). Next, to identify alternative splice events in adult zebrafish tissues including bone, we analyzed VastDB, a large database of alternative splice events estimated using transcriptomic profiles from different cell/tissue types [39]. Alternative splice events characterized by VastDB include cassette exons and microexons, alternative 5′ and 3′ splice site choices, and intron retention. Our query of VastDB revealed no alternative splice events for zebrafish *cped1* meeting a minimum threshold of alternative usage. Maynard et al. previously showed that *Cped1* exon expression varies during osteoblast differentiation, suggesting that alternative splicing varies during this process [1]. Previously, our lab conducted an analysis of alternatively spliced transcripts in *sp7*+ osteoblasts during zebrafish fin regeneration [40]. Using VAST-TOOLS [39] and a public RNA-seq dataset [41], we identified 1144 alternative splicing events differentially observed between 0 and 4 days post amputation [40]. We searched the results of this analysis and found no alternative splicing events for *cped1*. Taken together, our analyses fail to support alternative splice events involving exon skipping for zebrafish *cped1* that are similar to events that occur for mouse *Cped1*. Thus, when referring to *cped1* gene expression below, we assume results are for transcripts harboring all 21 exons unless otherwise noted.

cped1 is expressed in multiple cell/tissue types

To determine *cped1* expression patterns during zebrafish embryonic development, we analyzed a publicly available single-cell RNA-sequencing (scRNA-seq) dataset by Saunders et al. [26] which profiled 1,223 zebrafish embryos collected from 19 timepoints between 18 and 96 hours post fertilization (hpf), to assess *cped1* gene expression in the 156 annotated cell clusters (Fig 1B). An unknown cluster of cells marked by $dcn^{+}/col6^{+}$ expression exhibited the highest level of *cped1* expression (average expression = 6.24). Moderate *cped1* expression in the osteoblast cell cluster was observed (average expression = 1.149). With regard to other annotated cell clusters, we found that *cped1* expression was prominent in muscle and muscle progenitor cell clusters, mesenchymal cells, and cells in the pharyngeal arch. Thus, *cped1* is broadly expressed in multiple cell types, including moderate expression in osteoblasts.

To determine *cped1* expression in adult tissues, we queried the VASTDB database [39], which collates bulk RNA-sequencing for a variety of adult zebrafish tissues. VASTDB reported the highest

expression of *cped1* in swim bladder (12.80 cRPKM) and heart (10.71 cRPKM), with moderate expression of *cped1* in bone (3.15 cRPKM) (Fig 1C). Next, we examined the distribution of *cped1* expression in wildtype adult zebrafish using RT-PCR. Primers were designed to amplify a region spanning exons 14 through 16, and RT-PCR was performed on cDNA from nine solid organ tissues (Fig 1D). All PCR products were confirmed by Sanger sequencing. Highest *cped1* expression was detected in tissues from the swim bladder, heart, and eyes. We also observed moderate *cped1* expression in the skin, intestines, and testes. *cped1* expression was only faintly detectable in muscle and brain tissues, and virtually undetectable in vertebral bone. Notably, moderate levels of *cped1* were detected in bone by RNA-sequencing in VASTDB, thus it is possible that *cped1* transcript levels in vertebral bone, while present, are too low to be detected in our RT-PCR assay. Taken together, our results suggest that *cped1* is broadly expressed in multiple adult tissues, with moderate or low expression in bone.

Fig 1. Characterization of *cped1* expression. (A) Alternative splicing events for *cped1*. Top: Exon-intron maps for the two *cped1* transcript isoforms. Bottom: Closeup views of exons 12, 17 and 19 show regions of these exons that vary in usage (denoted by the dotted red lines). The top two rows show how these exon regions differ between the two *cped1* transcript isoforms. The remaining rows show these exon regions at various stages of zebrafish development, from 2 cell stage up to 5 dpf, and are colored by usage, e.g. red indicates 100% usage in the exon, blue indicates 0% usage in the exon. Gray indicates no transcript evidence was detected at the specified developmental stage. Images for the three exonic regions were obtained from the MeDAS database [38], cropped, and assembled into a single image. (B-C) Barplots showing average *cped1* expression in multiple cell/tissue types. (B) *cped1* expression in zebrafish embryos/larvae, from the zebrafish scRNA-seq dataset published in [26]. The top 45 cell populations with the highest *cped1* expression are shown. Osteoblasts are highlighted by an arrow. (C) *cped1* expression in adult zebrafish, as reported in the VASTDB database [39]. Bone is highlighted by an arrow. (D) RT-PCR for *cped1* expression in tissues from wildtype adult fish. Primers amplified a region spanning exons 14 through 16. Amplification of *β-actin2* was performed in parallel and served as a loading control. Bone: Vertebral bone, Mus: Muscle, Int: Intestine, Brain: Whole brain, SB: Swim bladder, Test: Testes.

Characterization of the *cped1*^{sa20221} allele

To examine whether *cped1* is necessary for bone mass and morphology, we analyzed *cped1*^{sa20221} mutant zebrafish. The *cped1*^{sa20221} allele was generated as part of the Wellcome Sanger Institute's ENU mutagenesis project [42]. The allele harbors a single point mutation (ENSDART00000143690.1:c.1922C>A; p.Ser641*) that is predicted to result in a premature stop codon in exon 15 of the zebrafish Cped1 protein. Exon 15 maps to a region upstream of the predicted PC-esterase domain of the protein, thus, translation of the predicted truncated transcript should result in loss of the PC-esterase domain (Fig 2A). To determine the effects of the premature stop codon on the transcript, we performed RT-PCR spanning the exons flanking the mutation-harboring exon using tissues from adult homozygous mutants (which we henceforth refer to as *cped1*^{sa20221} mutants) and wildtype clutchmates. We found that the expression level of the *cped1* transcript was visibly reduced in *cped1*^{sa20221} mutants compared to wildtype (Fig 2C), suggesting that the mutant transcript is degraded by nonsense-mediated decay (NMD). While CRISPR-induced indels have been shown to generate novel splice variants that can help protect against deleterious mutations [43], we did not observe evidence of exon skipping resulting in loss of exon 15 in *cped1*^{sa20221} mutants. Based on the reduced *cped1* transcript in *cped1*^{sa20221} mutants, as well as the predicted loss of the PC-esterase domain, we conclude that *cped1*^{sa20221} is likely to be functioning as a strong hypomorph or null allele.

Fig 2. Characterization of the *cped1*^{sa20221} allele. (A) Sequence and genomic location of *sa20221*. Blue highlighted regions indicate the locations of the exonic regions encoding for the cadherin-like domain and PC-esterase domain. (B) Predicted effects of *sa20221* on Cped1 amino acid sequence. For (A) and (B), information for *w1003*, an allele we previously described [15], is shown for reference. (C) Mutant mRNA is degraded in *cped1*^{sa20221} mutants. RT-PCR for the region spanning exons 14 through 16 of *cped1* in adult whole body tissues shows reduced transcript levels in *cped1*^{sa20221} mutants compared to controls. Evidence of exon skipping in exon 15 was not observed.

***cped1*^{sa20221} mutants exhibit normal vertebral bone mass and morphology**

To determine whether *cped1* is necessary for bone mass and morphology, we performed deep vertebral bone phenotyping in adult *cped1*^{sa20221} mutants. Adult *cped1*^{sa20221} mutants and wildtype clutchmates were collected at 90 dpf and scanned by microCT (n=8 per group). We used FishCuT to assess 200 measures of vertebral bone mass, morphology, and mineral density [31]. Briefly, vertebrae of each fish were divided into three anatomical compartments (centrum, haemal arch, and neural arch) that were analyzed for three measurements (volume, tissue mineral density (TMD), and thickness), resulting in nine distinct vertebral metrics. With the addition of centrum length, we obtained a total of 10 measurements for each analyzed vertebra (20 vertebrae in total). A standard score was computed for each measurement, and the scores were color-coded and arranged into matrices that we call "skeletal barcodes" (Fig 3A). We then plotted the 10 measurements as a function of vertebral number along the axial skeleton and calculated p-values using the global test (Fig 3B-K). No significant differences in any of the measurements were found between *cped1*^{sa20221} mutants and their controls. Finally, we did not observe obvious differences in *cped1*^{sa20221} mutants and controls when assessing for gross vertebral phenotypes such as vertebrae number, rib fracture calluses, neural arch non-unions, centrum fusion, or centrum compressions (Fig 3L). Thus, our studies in *cped1*^{sa20221} fail to support a role of *cped1* in adult vertebral bone mass and morphology.

Fig 3. *cped1*^{sa20221} mutants exhibit normal vertebral bone mass and morphology. (A) Skeletal barcodes for *cped1*$^{+/+}$ and *cped1*^{sa20221} mutants (3 fish/group shown) visually depict individual vertebral phenomes. (B–K) Vertebral phenotypic measures (indicated by the graph title, with units for y axis) plotted as a function of vertebra along the spine. Values are depicted mean ± SEM (n=8/group). No measures with $p<0.05$ in the global test were detected. Cent, centrum; Haem, haemal arch; Neur, neural arch; Vol, volume; TMD, tissue mineral density; Th, thickness; Le, length. (L) Maximum intensity projections of microCT scans.

Loss of *cped1* does not affect vertebral bone mass and morphology in multiple mutant lines

While our studies did not reveal a vertebral phenotype in *cped1*^{sa20221} mutants, it is possible that the allele has unintended consequences on Cped1 function. Thus, we sought to repeat our analyses using a different *cped1* mutant allele. For this, we analyzed *cped1*^{w1003} mutants [15]. As described in Watson et al., *cped1*^{w1003} harbors a CRISPR/Cas9-induced net 11 bp deletion (c.831-844delinsACT). This indel mutation causes a frameshift and premature stop codon in exon 6 (ENSDARP00000067250.4, p:Gln278Leu;fs*5) which is predicted to result in truncation of the Cped1 protein and loss of both the cadherin-like and PC-esterase domains (Fig 2B). Notably, normal levels of mutant *cped1* transcript are observed in *cped1*^{w1003} mutants [15]. Thus, transcriptional adaptation caused by mutant mRNA degradation, a form of genetic compensation that can produce mild or even an absence of expected phenotypes [44], is unlikely. We previously showed that adult *cped1*^{w1003} mutants do not exhibit significant differences in lean mass-related traits when compared to their wildtype siblings [15]. However, deep vertebral phenotyping using FishCuT in *cped1*^{w1003} mutants was not performed in the study of Watson et al. [15].

We performed FishCuT vertebral analysis in adult (90 dpf) *cped1*^{w1003} mutants. We observed no significant differences between c*ped1*^{w1003} mutants and their wildtype clutchmates (S1 Fig). Next, we combined data for c*ped1*^{w1003} and *cped1*^{sa20221} mutant lines in a two-way ANOVA analysis (Fig 4). We surmised that by combining data for both lines into a single analysis, this would increase our power to detect smaller effect sizes. For this, we used the average of each of the 10 FishCuT measurements across the 16 rostral-most measured vertebrae for both mutant alleles (we chose to analyze 16 rather than 20 vertebrae for this analysis because only 16 vertebrae were analyzed for *cped1*^{w1003} mutants in [15]). The two-way ANOVA allowed us to simultaneously determine whether (i) there were common phenotypic differences between wildtype and mutants for both alleles (indicated by p-value for genotype), (ii) there were baseline phenotypic differences for different alleles due to genetic background and/or environmental conditions when testing each allele (indicated by p-value for allele), and (iii) mutants for each *cped1* allele exhibited different phenotypic responses when compared to wildtype (indicated by p-value for genotype:allele interaction).

Fig 4. Loss of *cped1* does not affect vertebral bone mass and morphology in multiple mutant lines. (A-J) Combined analysis of vertebral measurements for *cped1*^{sa20221} and *cped1*^{w1003} mutants compared to their respective wildtype clutchmates. Each point represents a single fish, and the value is the average of

16 measured vertebrae. Bars indicate mean ± SEM. Shown are p-values from Sidak's multiple comparisons tests; no significant p-values for comparisons between homozygous mutants and respective controls were observed.

The result of the two-way ANOVA indicated that there were no significant effects of genotype (i.e., wildtype versus mutant) for any of the vertebral measurements (Table 1). Moreover, Sidak's multiple comparisons analysis for each allele found no significant differences between wildtype and mutant for either allele. We also observed no statistically significant interactions between allele and genotype, indicating that mutants for each *cped1* allele exhibited similar phenotypic responses when compared to wildtype. Several measures had p-values <0.05 for the allele factor, indicating there were baseline phenotypic differences for different alleles. Because the *cped1*^{w1003} fish was generated in an AB background, whereas the *cped1*^{sa20221} fish was generated in a longfin background, significant effects of allele are likely attributable to (i) background differences between the two lines and/or (ii) differences in environmental conditions that equally impacted controls and mutants for each allele (e.g., different rates of developmental progress). In sum, our studies in multiple *cped1* mutant lines fail to support a role of *cped1* in vertebral bone mass and morphology.

Table 1. P-values from two-way ANOVA of vertebral measures in *cped1*^{sa20221} and *cped1*^{w1003} mutants and respective wildtype controls.

Measurement	Genotype	Allele	Interaction
centrum volume	p=0.503	p=0.298	p=0.283
centrum thickness	p=0.3901	p=0.112	p=0.903
centrum TMD	p=0.612	p=0.029*	p=0.207
centrum length	p=0.638	p=0.262	p=0.117
haemal arch volume	p=0.3403	p=0.0020*	p=0.1966
haemal arch thickness	p=0.5184	p=0.0339*	p=0.251
haemal arch TMD	p=0.582	p=0.0816	p=0.1229
neural arch volume	p=0.3609	p=<0.0001*	p=0.3076
neural arch thickness	p=0.4067	p=0.027*	p=0.8259
neural arch TMD	p=0.5106	p=0.1223	p=0.4574

* = p-value < 0.05

Loss of *cped1* does not affect lean tissue mass and morphology

Because variants at the *CPED1-WNT16* locus have been associated with pleiotropic effects on both bone and lean mass-related traits [15, 45], we also examined whether *cped1*^{sa20221} mutants exhibited any phenotypic differences in lean tissue mass and morphology. For this, we measured the following traits: standard length and fineness ratio to assess body shape; total, anterior and posterior trunk lean volumes; and anterior and posterior swim bladder chamber length [15]. We also manually measured centrum length, neural arch length, and neural arch angle, respectively, since these measures are highly correlated to myomere length, height, and angle, respectively [46]. We previously found no significant differences in these measures in *cped1*^{w1003} mutants [15]. We combined data for both *cped1*^{sa20221} and *cped1*^{w1003} and performed a two-way ANOVA analysis. There were no statistically significant effects of genotype in any of the muscle morphology measures between controls and germline mutants (Fig 5). Furthermore, for each allele, Sidak's multiple comparisons tests did not detect significant differences between wildtype and mutant. There were also no significant genotype:allele interactions for any of the measures. Finally, statistically significant p-values for the allele factor were detected for several measures, which we again attributed to the different backgrounds of the two lines and/or environmental differences when testing each allele (Table 2). Taken together, our findings fail to support a role of *cped1* in lean tissue mass and morphology.

Fig 5. Loss of *cped1* does not affect lean mass morphology. (A-I) Combined analysis of lean mass-related measures for *cped1*^{sa20221} and *cped1*^{w1003} mutants and their corresponding wildtype clutchmates. Each point represents a single fish. Bars indicate mean ± SEM. Shown are p-values from Sidak's multiple

comparisons tests; no significant p-values for comparisons between homozygous mutants and their respective controls were observed.

Table 2. P-values from two-way ANOVA of lean mass-related traits in *cped1*^{sa20221} and *cped1*^{w1003} mutants and respective wildtype controls.

Measurement	Genotype	Allele	Interaction
standard length	p=0.4611	p=0.7151	p=0.2968
fineness ratio	p=0.8016	p=<0.0001*	p=0.7561
neural arch length	p=0.798	p=0.0005*	p=0.8302
neural arch angle	p=0.5998	p=0.7910	p=0.7660
ant. swim bladder chamber	p=0.3921	p=0.2103	p=0.9082
pos. swim bladder chamber	p=0.238	p=0.6046	p=0.7150
ant. trunk lean volume	p=0.4556	p=0.0003*	p=0.8574
pos. trunk lean volume	p=0.8381	p=0.0011*	p=0.6902
total trunk lean volume	p=0.6658	p=0.0005*	p=0.7515

* = p-value < 0.05

Loss of *cped1* does not affect craniofacial morphology

Several GWA studies have suggested that variants in the intronic region of *CPED1* may influence human craniofacial morphology. For instance, Medina-Gomez et al. found that variants most strongly associated with skull BMD were located in the intronic region of *CPED1*, with rs7801723 identified as the most significantly associated SNP [5]. Moreover, in a GWA study identifying human genomic loci associated with craniofacial morphology in a Latin American population, Bonfante et al. detected a single nucleotide variant in the intronic region of the *CPED1* gene (rs6950680) associated with “jaw protrusion” [47]. To assess whether *cped1* zebrafish mutants exhibited altered craniofacial morphology, we performed landmark-based morphometric analyses using methods we have previously described [34, 35]. Using the Markups module in 3D Slicer [36], we manually placed 13 markers on distinctive craniofacial landmarks of microCT scans of *cped1*^{sa20221} and *cped1*^{w1003} mutants and their respective wildtype clutchmates, and measured the distances between 7 pairs of landmarks (Fig. 6A, B). From our two-way ANOVA analysis, we did not find any significant effects of genotype for any of the craniofacial measurements (Fig. 6C-I and Table 3). In addition, Sidak’s multiple comparisons test did not detect significant differences between homozygous mutants and their respective wildtype controls for either allele. Moreover, no significant interactions were found between genotype and allele. For reasons described previously, statistically significant p-values for the allele factor were detected for several measures similar to previous analyses. In sum, our findings fail to support a role of *cped1* in craniofacial morphology.

Fig 6. Loss of *cped1* does not affect craniofacial morphology. (A) Anatomical landmarks used for measurements. Shown are the lateral view (left) and dorsal view (right) of a wildtype zebrafish skull. Landmark positions are labeled in blue. Note that landmark 11 is on the right lateral surface, opposite landmark 6, and landmark 13 is on the right lateral surface, opposite landmark 8. (B) Distances between pairs of landmarks were used as measurements to quantify craniofacial morphology. (C-I) Combined analysis of craniofacial morphological measures for *cped1*^{sa20221} and *cped1*^{w1003} mutants and their corresponding wildtype clutchmates. Each point represents an individual fish. Shown are p-values from Sidak’s multiple comparisons tests; no significant p-values for comparisons between homozygous mutants and controls were observed.

Table 3. P-values from two-way ANOVA of craniofacial phenotyping comparison of *cped1*^{sa20221} and *cped1*^{w1003} and their respective wildtype controls.

Measurement	Genotype	Allele	Interaction
skull length	p=0.566	p=0.922	p=0.1485
frontal/parietal bone length	p=0.526	p=0.218	p=0.223

epiphyseal bar length	p=0.629	p=0.243	p=0.389
distance between anguloarticulars	p=0.643	p=0.0409*	p=0.312
midline skull width	p=0.099	p=0.0009*	p=0.177
dorsal skull width	p=0.252	p=0.404	p=0.374
ventral skull width	p=0.976	p=0.0089*	p=0.205

* = p-value < 0.05

The PC-esterase domain in zebrafish Cped1 lacks a conserved catalytic domain

Our results so far showed negligible effects on bone and lean mass morphology arising from two different nonsense mutations in *cped1*. These findings are in contrast to previous studies in *Cped1* mutant mice showing a role of *Cped1* in contributing to bone strength [20], leading us to ask whether the functional activity of the PC-esterase domain is conserved in zebrafish. We therefore decided to compare the Cped1 amino acid sequence of zebrafish to CPED1 orthologs in other chordates. We used the MUSCLE alignment software to perform a multiple sequence alignment of CPED1 orthologs identified from the NCBI Orthologs database: human (NP_079189.4), mouse (*Mus musculus*, NP_001074820.1), chicken (*Gallus gallus*, XP_416005.4), frog (*Xenopus tropicalis*, XP_031754845.1), lizard (*Sceloporus undulatus*, XP_042324422.1), amphioxus (*Branchiostoma floridae*, XP_035676865.1), little skate (*Leucoraja erinacea*, XP_055506810.1), and another teleost, Japanese medaka (*Oryzias latipes*, XP_023808151.1). We also performed a BLASTp search for a Cped1 ortholog in the basal chordate *Ciona intestinalis* in the non-redundant protein sequences database on NCBI but did not recover any potential orthologs. The alignment showed that, compared to the human and mouse orthologs, zebrafish Cped1 shares 39.87% and 38.92% identity over the entire protein sequence, respectively. Within the predicted PC-esterase domain, zebrafish Cped1 shares 55.6% and 54.28% identity with human and mouse orthologs, respectively (Fig 7), indicating that the PC-esterase domain is more highly conserved between zebrafish and mammals than other regions of the protein.

We then asked whether the predicted enzymatic active site of the PC-esterase domain was intact in zebrafish. To date, the crystal structure and biochemical characterization of only one member of the PC-esterase domain family has been determined, XOAT1 from *Arabidopsis thaliana* [18, 48]. The crystal structure of XOAT1 revealed the presence of a canonical “catalytic triad” of amino acids adjacent to the active site (Serine-Aspartate-Histidine), which was required for the enzymatic activity of the protein as determined by site-directed mutagenesis studies. The biochemical mechanism of the catalytic triad is well characterized and typically consists of a serine (S) in a GDS motif, and an aspartate (D) and histidine (H) in a DxxH motif found upstream of the last predicted helix [17, 49]. Anantharaman and Aravind previously showed that, within this catalytic triad, the serine and histidine (but not aspartate) showed absolute conservation amongst representatives of the PC-esterase family [17]. Using the positions of the predicted catalytic residues, we identified the corresponding residues in our alignment (asterisks in Fig 7) and found that the predicted catalytic triad appears to be disrupted in zebrafish. Specifically, we observed that the histidine residue which showed absolute conservation amongst the PC-esterase family in the study of [17] was substituted with a glutamine (Q) in zebrafish. This substitution was not seen in any other sequence we analyzed. During ester bond cleavage, the histidine in the catalytic triad facilitates the chemical reaction by removing a proton from the serine, thereby activating the serine and allowing it to attack the ester bond [18, 50]. It is therefore plausible that loss of the histidine in zebrafish disrupts the enzymatic activity of the PC-esterase domain in Cped1.

Fig 7. Multiple sequence alignment of the predicted PC-esterase domain of CPED1 orthologs from chordate species. Individual residues are colored based on side chain chemistry. The consensus sequence is shown below the alignment and is composed of the amino acid residues with the highest frequency at each position, with the most highly conserved residues denoted by darker, taller bars. The catalytic triad of amino acid residues is denoted with asterisks, and the GDS motif is indicated with a black box. The histidine residue which showed absolute conservation amongst the PC-esterase family in the study of [17] and which was substituted with a glutamine (Q) in zebrafish (*D. rerio*) is indicated with an arrow.

Do *CPED1* orthologs have different roles in zebrafish and mouse bone?

Our analyses indicate potential differences between zebrafish and mouse *CPED1* orthologs at the gene expression and protein levels. At the level of gene expression, mouse *Cped1* exhibits exon skipping as well as expression of N- and C-terminally truncated isoforms. In contrast, alternative splicing of zebrafish *cped1* appears to primarily consist of alternative donor/acceptor sites. Because our analyses fail to support alternatively spliced *cped1* transcripts with missing exons, both mutant alleles in our study are expected to impact all *cped1* isoforms, allowing for a less ambiguous assessment of the role of *cped1* in bone. This is in contrast to exon skipping observed for mouse *Cped1*, which makes the generation of CRISPR-induced knockout alleles more challenging. We acknowledge that, if exon skipping is critical to *CPED1*'s regulation of bone in humans, the absence of this in zebrafish *cped1* could make it an inappropriate model. In this context, it is worthwhile to note that exon skipping for exon 3 in mouse *Cped1*, which is catalogued in the VASTDB and MeDAS databases, is not predicted by VASTDB to be conserved in the orthologous human or zebrafish exons. At the level of the encoded protein, we found that zebrafish Cped1 is predicted to harbor an amino acid substitution for a key residue within the catalytic triad of the PC-esterase domain, a substitution which is not observed in mouse, human, or any other representative of the PC-esterase family in the study of [17]. Even though the functional domains of CPED1 have not yet been determined experimentally, the loss of a putative catalytic amino acid in the predicted PC-esterase domain of zebrafish Cped1 suggests that the protein's function may have been lost during evolution. Taken together, there are predicted transcriptional and protein differences in *CPED1* zebrafish and mouse orthologs that could underlie their different roles in bone.

Does *CPED1* influence BMD and fracture risk heritability at the *CPED1-WNT16* locus?

While we acknowledge that the role of zebrafish *cped1* in bone may be different than the role of *CPED1* in mammals, it is worthwhile to note that our findings share some similarities with previous functional studies. In particular, our studies fail to support an essential role of *cped1* in bone, which is in agreement with studies by Chesi et al. who found that *CPED1* knockdown did not alter BMP2-induced osteoblastic differentiation in primary human MSCs [16]. In addition, *Cped1* mutant mice analyzed by the International Mouse Phenotyping Consortium did not exhibit any significant bone phenotypes (www.mousephenotype.org) [51]. These mice also did not exhibit any significant differences in lean mass or craniofacial-related measures. These studies bring forth the question of whether the *CPED1-WNT16* locus could influence BMD and fracture independently of *CPED1*. Other genes at 7q31.31 (*ING3*, *FAM3C*, and *WNT16*) have previously been shown to have a role in regulating bone morphology and strength and/or osteoblast differentiation. For example, Chesi et al. found that siRNA-mediated knockdown of *ING3* in primary hMSCs reduced BMP2-induced osteogenic differentiation, suggesting that ING3 is needed for osteoblast differentiation [16]. In studies by Maata et al. and Bendre et al., *FAM3C* was shown to be important for bone morphology in mouse, and in mediating alkaline phosphatase expression during osteoblastic differentiation [52, 53]. Finally, a large body of evidence has shown that *WNT16* is likely a causal gene at the locus. For example, *Wnt16* is required for cortical bone mass and strength in mice [5, 6, 11, 12, 54-58], and in humans, expression levels of *WNT16* from iliac crest samples were positively correlated with measures of BMD at multiple skeletal sites including total body, skull, legs, total hip, and lumbar spine [5]. In addition, higher levels of *WNT16* expression were correlated with higher total body lean mass (TBLM) and BMD, suggesting that *WNT16* has pleiotropic effects on BMD and lean mass. This finding was supported by a bivariate GWAS meta-analysis in a pediatric cohort that identified the *CPED1-WNT16* locus as harboring the lead variant most significantly associated with TBLM and total body less head-BMD. This finding was also supported by our recent study showing that (i) *wnt16* is specifically expressed in dermomyotome and notochord, structures critical for the development of muscle and the spine, respectively, and (ii) *wnt16*$^{-/-}$ zebrafish mutants exhibited altered vertebral bone morphology and lean mass and morphology [15]. Thus, although it cannot be ruled out that *CPED1* does not influence bone and lean mass in humans, there are multiple candidate genes in this locus that could play an equal or larger role in influencing musculoskeletal traits.

Limitations

There are some limitations to our study. First, while we found no effects of loss of *cped1* in 90 dpf adult bone, it cannot be ruled out that its loss affects bone at a later stage (e.g., in aged animals). It is also possible that *cped1* plays a critical role in tissues and structures in zebrafish that we did not analyze. Additional analyses of other tissues are warranted, especially in tissues exhibiting strong *cped1* expression such as the heart and swim bladder. Second, as mentioned previously, it is possible that genetic compensation could reduce the effects of *cped1* loss in zebrafish. Our studies do not support genetic compensation arising from transcriptional adaptation due to mutant mRNA degradation or removal of the PTC-harboring exon (exon skipping). However, other forms of genetic compensation can occur, for example, through cryptic splice sites, cryptic start sites, or intron inclusion [59-65]. While we cannot exclude these possibilities, our analysis of two independent *cped1* zebrafish lines harboring mutations in different exons makes it less likely that our results are due to the same compensatory effects. Lastly, while reduced bone strength in *Cped1* mutant mice was reported in males, it is possible this phenotype is sex-dependent. Our studies were not designed to include sex as a biological variable, precluding us from determining whether results differed with sex. However, it is noteworthy that the association between BMD and the *CPED1-WNT16* locus does not show significant evidence of sex-specificity [4], suggesting that if *CPED1* acts as a causal gene at the locus, the mechanism by which it contributes to BMD is unlikely to exhibit significant sexual dimorphism.

Acknowledgements

Research reported in this publication was supported by the National Institute of Arthritis and Musculoskeletal and Skin Diseases of the National Institutes of Health under Award Number AR074417 as well as the Office of the Director (OD). AEG was supported by the National Institute on Aging of the National Institutes of Health, under Award Number AG066574, the Biological Mechanisms for Healthy Aging Training Grant. The content is solely the responsibility of the authors and does not necessarily represent the official views of the National Institutes of Health. The authors have no relevant financial or non-financial interests to disclose.

References

1. Maynard RD, Godfrey DA, Medina-Gomez C, Ackert-Bicknell CL. Characterization of expression and alternative splicing of the gene cadherin-like and PC esterase domain containing 1 (Cped1). Gene. 2018;674:127-33.
2. Cho YS, Go MJ, Kim YJ, Heo JY, Oh JH, Ban HJ, et al. A large-scale genome-wide association study of Asian populations uncovers genetic factors influencing eight quantitative traits. Nat Genet. 2009;41(5):527-34.
3. Zhang LS, Hu HG, Liu YJ, Li J, Yu P, Zhang F, et al. A follow-up association study of two genetic variants for bone mineral density variation in Caucasians. Osteoporos Int. 2012;23(7):1867-75.
4. Estrada K, Styrkarsdottir U, Evangelou E, Hsu YH, Duncan EL, Ntzani EE, et al. Genome-wide meta-analysis identifies 56 bone mineral density loci and reveals 14 loci associated with risk of fracture. Nat Genet. 2012;44(5):491-501.
5. Medina-Gomez C, Kemp JP, Estrada K, Eriksson J, Liu J, Reppe S, et al. Meta-analysis of genome-wide scans for total body BMD in children and adults reveals allelic heterogeneity and age-specific effects at the WNT16 locus. PLoS Genet. 2012;8(7):e1002718.
6. Zheng HF, Tobias JH, Duncan E, Evans DM, Eriksson J, Paternoster L, et al. WNT16 influences bone mineral density, cortical bone thickness, bone strength, and osteoporotic fracture risk. PLoS Genet. 2012;8(7):e1002745.
7. Koller DL, Zheng HF, Karasik D, Yerges-Armstrong L, Liu CT, McGuigan F, et al. Meta-analysis of genome-wide studies identifies WNT16 and ESR1 SNPs associated with bone mineral density in premenopausal women. J Bone Miner Res. 2013;28(3):547-58.
8. Morris JA, Kemp JP, Youlten SE, Laurent L, Logan JG, Chai RC, et al. An atlas of genetic influences on osteoporosis in humans and mice. Nat Genet. 2019;51(2):258-66.

9. Kemp JP, Morris JA, Medina-Gomez C, Forgetta V, Warrington NM, Youlten SE, et al. Identification of 153 new loci associated with heel bone mineral density and functional involvement of GPC6 in osteoporosis. Nat Genet. 2017;49(10):1468-75.
10. Gomez AE, Addish S, Alvarado K, Boatemaa P, Onyali AC, Ramirez EG, et al. Multiple Mechanisms Explain Genetic Effects at the CPED1-WNT16 Bone Mineral Density Locus. Curr Osteoporos Rep. 2023;21(2):173-83.
11. Moverare-Skrtic S, Henning P, Liu X, Nagano K, Saito H, Borjesson AE, et al. Osteoblast-derived WNT16 represses osteoclastogenesis and prevents cortical bone fragility fractures. Nat Med. 2014;20(11):1279-88.
12. Wergedal JE, Kesavan C, Brommage R, Das S, Mohan S. Role of WNT16 in the regulation of periosteal bone formation in female mice. Endocrinology. 2015;156(3):1023-32.
13. Qu X, Liao M, Liu W, Cai Y, Yi Q, Long J, et al. Loss of Wnt16 Leads to Skeletal Deformities and Downregulation of Bone Developmental Pathway in Zebrafish. Int J Mol Sci. 2021;22(13).
14. McGowan LM, Kague E, Vorster A, Newham E, Cross S, Hammond CL. Wnt16 Elicits a Protective Effect Against Fractures and Supports Bone Repair in Zebrafish. JBMR Plus. 2021;5(3):e10461.
15. Watson CJ, Tang WJ, Rojas MF, Fiedler IAK, Morfin Montes de Oca E, Cronrath AR, et al. wnt16 regulates spine and muscle morphogenesis through parallel signals from notochord and dermomyotome. PLoS Genet. 2022;18(11):e1010496.
16. Chesi A, Wagley Y, Johnson ME, Manduchi E, Su C, Lu S, et al. Genome-scale Capture C promoter interactions implicate effector genes at GWAS loci for bone mineral density. Nat Commun. 2019;10(1):1260.
17. Anantharaman V, Aravind L. Novel eukaryotic enzymes modifying cell-surface biopolymers. Biol Direct. 2010;5:1.
18. Anderson AC, Stangherlin S, Pimentel KN, Weadge JT, Clarke AJ. The SGNH hydrolase family: a template for carbohydrate diversity. Glycobiology. 2022;32(10):826-48.
19. Ackert-Bicknell C, Schilling K, Godfrey DA, Ottenberg G, Liu Q, Maynard R. Cped1 impacts osteoblast mediated extracellular matrix production in an isoform specific manner [abstract]. American Society for Bone and Mineral Research; Sep 2022; Austin, TX: Journal of Bone and Mineral Research; 2022. p. 1-364.
20. Wang Y, Godfrey D, Maynard R, Szeto N, Butler V, David M, et al. Allelic Effects at the Cped1 Locus Interact with Parathyroid Hormone to Impact Bone Strength in Mice [abstract]. American Society for Bone and Mineral Research; Nov 2023; Vancouver, BC: Journal of Bone and Mineral Research; 2023. p. 1545-2024.
21. Kwon RY, Watson CJ, Karasik D. Using zebrafish to study skeletal genomics. Bone. 2019;126:37-50.
22. Busse B, Galloway JL, Gray RS, Harris MP, Kwon RY. Zebrafish: An Emerging Model for Orthopedic Research. J Orthop Res. 2020;38(5):925-36.
23. Tonelli F, Bek JW, Besio R, De Clercq A, Leoni L, Salmon P, et al. Zebrafish: A Resourceful Vertebrate Model to Investigate Skeletal Disorders. Front Endocrinol (Lausanne). 2020;11:489.
24. Henke K, Farmer DT, Niu X, Kraus JM, Galloway JL, Youngstrom DW. Genetically engineered zebrafish as models of skeletal development and regeneration. Bone. 2023;167:116611.
25. Gupta T, Mullins MC. Dissection of organs from the adult zebrafish. J Vis Exp. 2010(37).
26. Saunders LM, Srivatsan SR, Duran M, Dorrity MW, Ewing B, Linbo TH, et al. Embryo-scale reverse genetics at single-cell resolution. Nature. 2023;623(7988):782-91.
27. Trapnell C, Cacchiarelli D, Grimsby J, Pokharel P, Li S, Morse M, et al. The dynamics and regulators of cell fate decisions are revealed by pseudotemporal ordering of single cells. Nat Biotechnol. 2014;32(4):381-6.
28. Butler A, Hoffman P, Smibert P, Papalexi E, Satija R. Integrating single-cell transcriptomic data across different conditions, technologies, and species. Nat Biotechnol. 2018;36(5):411-20.
29. RCoreTeam. R: A language and environment for statistical computing 2022 [Available from: https://www.R-project.org/.
30. Watson CJ, Monstad-Rios AT, Bhimani RM, Gistelinck C, Willaert A, Coucke P, et al. Phenomics-Based Quantification of CRISPR-Induced Mosaicism in Zebrafish. Cell Syst. 2020;10(3):275-86 e5.

31. Hur M, Gistelinck CA, Huber P, Lee J, Thompson MH, Monstad-Rios AT, et al. MicroCT-based phenomics in the zebrafish skeleton reveals virtues of deep phenotyping in a distributed organ system. Elife. 2017;6.
32. Gomez AE, Salmon P, Baumgarten N, Rai J, Huber P, Simmonds SP, et al. MicroCT scanning and analysis in the zebrafish skeleton. Protocol Exchange. 2024.
33. Schindelin J, Arganda-Carreras I, Frise E, Kaynig V, Longair M, Pietzsch T, et al. Fiji: an open-source platform for biological-image analysis. Nat Methods. 2012;9(7):676-82.
34. Diamond KM, Rolfe SM, Kwon RY, Maga AM. Computational anatomy and geometric shape analysis enables analysis of complex craniofacial phenotypes in zebrafish. Biol Open. 2022;11(2).
35. Diamond KM, Burtner AE, Siddiqui D, Alvarado K, Leake S, Rolfe S, et al. Examining craniofacial variation among crispant and mutant zebrafish models of human skeletal diseases. J Anat. 2023;243(1):66-77.
36. Fedorov A, Beichel R, Kalpathy-Cramer J, Finet J, Fillion-Robin JC, Pujol S, et al. 3D Slicer as an image computing platform for the Quantitative Imaging Network. Magn Reson Imaging. 2012;30(9):1323-41.
37. Zhou L, Feng T, Xu S, Gao F, Lam TT, Wang Q, et al. ggmsa: a visual exploration tool for multiple sequence alignment and associated data. Brief Bioinform. 2022;23(4).
38. Li Z, Zhang Y, Bush SJ, Tang C, Chen L, Zhang D, et al. MeDAS: a Metazoan Developmental Alternative Splicing database. Nucleic Acids Res. 2021;49(D1):D144-D50.
39. Tapial J, Ha KCH, Sterne-Weiler T, Gohr A, Braunschweig U, Hermoso-Pulido A, et al. An atlas of alternative splicing profiles and functional associations reveals new regulatory programs and genes that simultaneously express multiple major isoforms. Genome Res. 2017;27(10):1759-68.
40. Tang WJ, Watson CJ, Olmstead T, Allan CH, Kwon RY. Single-cell resolution of MET- and EMT-like programs in osteoblasts during zebrafish fin regeneration. iScience. 2022;25(2):103784.
41. Lee HJ, Hou Y, Chen Y, Dailey ZZ, Riddihough A, Jang HS, et al. Regenerating zebrafish fin epigenome is characterized by stable lineage-specific DNA methylation and dynamic chromatin accessibility. Genome Biol. 2020;21(1):52.
42. Kettleborough RN, Busch-Nentwich EM, Harvey SA, Dooley CM, de Bruijn E, van Eeden F, et al. A systematic genome-wide analysis of zebrafish protein-coding gene function. Nature. 2013;496(7446):494-7.
43. Tuladhar R, Yeu Y, Tyler Piazza J, Tan Z, Rene Clemenceau J, Wu X, et al. CRISPR-Cas9-based mutagenesis frequently provokes on-target mRNA misregulation. Nat Commun. 2019;10(1):4056.
44. El-Brolosy MA, Kontarakis Z, Rossi A, Kuenne C, Gunther S, Fukuda N, et al. Genetic compensation triggered by mutant mRNA degradation. Nature. 2019;568(7751):193-7.
45. Medina-Gomez C, Kemp JP, Dimou NL, Kreiner E, Chesi A, Zemel BS, et al. Bivariate genome-wide association meta-analysis of pediatric musculoskeletal traits reveals pleiotropic effects at the SREBF1/TOM1L2 locus. Nat Commun. 2017;8(1):121.
46. Jayne BC, Lauder GV. Comparative morphology of the myomeres and axial skeleton in four genera of centrarchid fishes. J Morphol. 1994;220(2):185-205.
47. Bonfante B, Faux P, Navarro N, Mendoza-Revilla J, Dubied M, Montillot C, et al. A GWAS in Latin Americans identifies novel face shape loci, implicating VPS13B and a Denisovan introgressed region in facial variation. Sci Adv. 2021;7(6).
48. Lunin VV, Wang HT, Bharadwaj VS, Alahuhta M, Pena MJ, Yang JY, et al. Molecular Mechanism of Polysaccharide Acetylation by the Arabidopsis Xylan O-acetyltransferase XOAT1. Plant Cell. 2020;32(7):2367-82.
49. Gutteridge A, Thornton JM. Understanding nature's catalytic toolkit. Trends Biochem Sci. 2005;30(11):622-9.
50. Paetzel M, Dalbey RE. Catalytic hydroxyl/amine dyads within serine proteases. Trends Biochem Sci. 1997;22(1):28-31.
51. Groza T, Gomez FL, Mashhadi HH, Munoz-Fuentes V, Gunes O, Wilson R, et al. The International Mouse Phenotyping Consortium: comprehensive knockout phenotyping underpinning the study of human disease. Nucleic Acids Res. 2023;51(D1):D1038-D45.
52. Maatta JA, Bendre A, Laanti M, Buki KG, Rantakari P, Tervola P, et al. Fam3c modulates osteogenic cell differentiation and affects bone volume and cortical bone mineral density. Bonekey Rep. 2016;5:787.

53. Bendre A, Buki KG, Maatta JA. Fam3c modulates osteogenic differentiation by down-regulating Runx2. Differentiation. 2017;93:50-7.
54. Gori F, Lerner U, Ohlsson C, Baron R. A new WNT on the bone: WNT16, cortical bone thickness, porosity and fractures. Bonekey Rep. 2015;4:669.
55. Moverare-Skrtic S, Wu J, Henning P, Gustafsson KL, Sjogren K, Windahl SH, et al. The bone-sparing effects of estrogen and WNT16 are independent of each other. Proc Natl Acad Sci U S A. 2015;112(48):14972-7.
56. Alam I, Alkhouli M, Gerard-O'Riley RL, Wright WB, Acton D, Gray AK, et al. Osteoblast-Specific Overexpression of Human WNT16 Increases Both Cortical and Trabecular Bone Mass and Structure in Mice. Endocrinology. 2016;157(2):722-36.
57. Alam I, Oakes DK, Reilly AM, Billingsley C, Sbeta S, Gerard-O'Riley RL, et al. Overexpression of WNT16 Does Not Prevent Cortical Bone Loss Due to Glucocorticoid Treatment in Mice. JBMR Plus. 2019;3(4):e10084.
58. Alam I, Reilly AM, Alkhouli M, Gerard-O'Riley RL, Kasipathi C, Oakes DK, et al. Bone Mass and Strength are Significantly Improved in Mice Overexpressing Human WNT16 in Osteocytes. Calcif Tissue Int. 2017;100(4):361-73.
59. Anderson JL, Mulligan TS, Shen MC, Wang H, Scahill CM, Tan FJ, et al. mRNA processing in mutant zebrafish lines generated by chemical and CRISPR-mediated mutagenesis produces unexpected transcripts that escape nonsense-mediated decay. PLoS Genet. 2017;13(11):e1007105.
60. Sztal TE, McKaige EA, Williams C, Ruparelia AA, Bryson-Richardson RJ. Genetic compensation triggered by actin mutation prevents the muscle damage caused by loss of actin protein. PLoS Genet. 2018;14(2):e1007212.
61. San B, Rougeot J, Voeltzke K, van Vegchel G, Aben M, Andralojc KM, et al. The ezh2(sa1199) mutant zebrafish display no distinct phenotype. PLoS One. 2019;14(1):e0210217.
62. Buglo E, Sarmiento E, Martuscelli NB, Sant DW, Danzi MC, Abrams AJ, et al. Genetic compensation in a stable slc25a46 mutant zebrafish: A case for using F0 CRISPR mutagenesis to study phenotypes caused by inherited disease. PLoS One. 2020;15(3):e0230566.
63. Ma Z, Chen J. Premature Termination Codon-Bearing mRNA Mediates Genetic Compensation Response. Zebrafish. 2020.
64. Kontarakis Z, Stainier DYR. Genetics in Light of Transcriptional Adaptation. Trends Genet. 2020;36(12):926-35.
65. El-Brolosy MA, Stainier DYR. Genetic compensation: A phenomenon in search of mechanisms. PLoS Genet. 2017;13(7):e1006780.

Supporting information

S1 Table. Anatomical descriptions of the zebrafish craniofacial landmarks used for analysis.

S1 Fig. *cped1*^{w1003} mutants exhibit normal vertebral bone mass and morphology. Vertebral phenotypic measures (indicated by the graph title, with units for y axis in parentheses) plotted as a function of vertebra along the spine. Values are depicted as mean ± SEM (n=8/group). No measures with $p<0.05$ in the global test were detected. Cent, centrum; Haem, haemal arch; Neur, neural arch; Vol, volume; TMD, tissue mineral density; Th, thickness; Le, length.

Figure 1

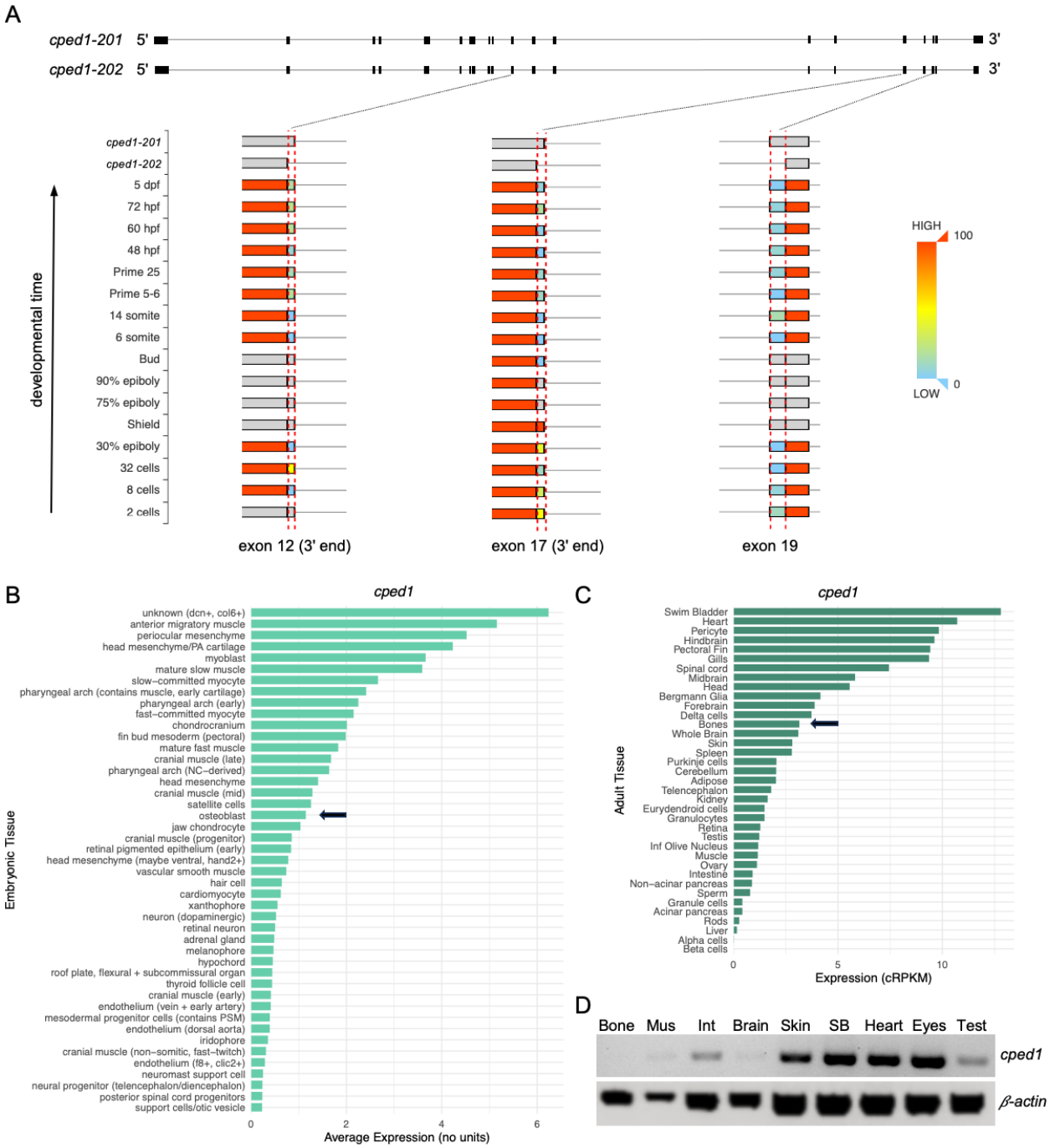
A
cped1-201 5' 3'
cped1-202 5' 3'
cped1-201
cped1-202
5 dpf
72 hpf
60 hpf
48 hpf
Prime 25
Prime 5-6
14 somite
6 somite
Bud
90% epiboly
75% epiboly
Shield
30% epiboly
32 cells
8 cells
2 cells
developmental time
HIGH
100
0
LOW
exon 12 (3' end)
exon 17 (3' end)
exon 19
B
cped1
Embryonic Tissue
unknown (dcn+, col6+)
anterior migratory muscle
periocular mesenchyme
head mesenchyme/PA cartilage
myoblast
mature slow muscle
slow−committed myocyte
pharyngeal arch (contains muscle, early cartilage)
pharyngeal arch (early)
fast−committed myocyte
chondrocranium
fin bud mesoderm (pectoral)
mature fast muscle
cranial muscle (late)
pharyngeal arch (NC−derived)
head mesenchyme
cranial muscle (mid)
satellite cells
osteoblast
jaw chondrocyte
cranial muscle (progenitor)
retinal pigmented epithelium (early)
head mesenchyme (maybe ventral, hand2+)
vascular smooth muscle
hair cell
cardiomyocyte
xanthophore
neuron (dopaminergic)
retinal neuron
adrenal gland
melanophore
hypochord
roof plate, flexural + subcommissural organ
thyroid follicle cell
cranial muscle (early)
endothelium (vein + early artery)
mesodermal progenitor cells (contains PSM)
endothelium (dorsal aorta)
iridophore
cranial muscle (non−somitic, fast−twitch)
endothelium (f8+, clic2+)
neuromast support cell
neural progenitor (telencephalon/diencephalon)
posterior spinal cord progenitors
support cells/otic vesicle
0
2
4
6
Average Expression (no units)
C
cped1
Adult Tissue
Swim Bladder
Heart
Pericyte
Hindbrain
Pectoral Fin
Gills
Spinal cord
Midbrain
Head
Bergmann Glia
Forebrain
Delta cells
Bones
Whole Brain
Skin
Spleen
Purkinje cells
Cerebellum
Adipose
Telencephalon
Kidney
Eurydendroid cells
Granulocytes
Retina
Testis
Inf Olive Nucleus
Muscle
Ovary
Intestine
Non−acinar pancreas
Sperm
Granule cells
Acinar pancreas
Rods
Liver
Alpha cells
Beta cells
0
5
10
Expression (cRPKM)
D
Bone
Mus
Int
Brain
Skin
SB
Heart
Eyes
Test
cped1
β-actin

Figure 2

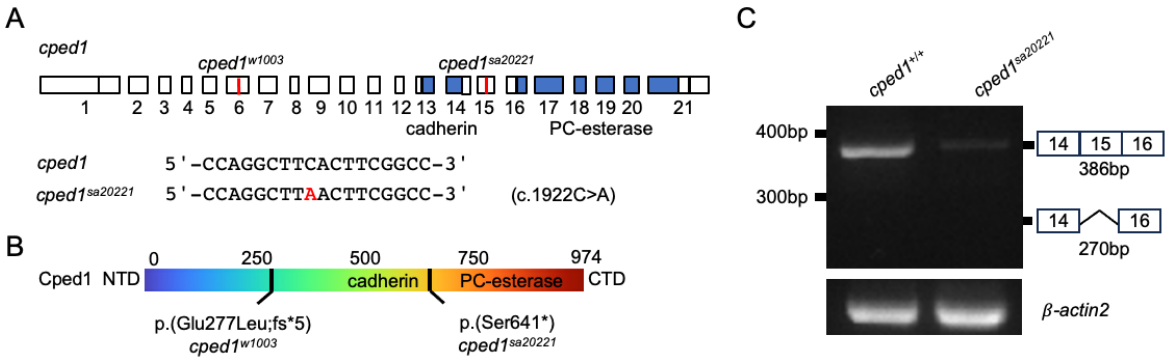
A
cped1
cped1w1003
cped1sa20221
1 2 3 4 5 6 7 8 9 10 11 12 13 14 15 16 17 18 19 20 21
cadherin
PC-esterase
cped1 5'-CCAGGCTTCACTTCGGCC-3'
cped1sa20221 5'-CCAGGCTTAACTTCGGCC-3' (c.1922C>A)
B
0 250 500 750 974
Cped1 NTD
cadherin
PC-esterase
CTD
p.(Glu277Leu;fs*5)
cped1w1003
p.(Ser641*)
cped1sa20221
C
cped1+/+
cped1sa20221
400bp
300bp
14 15 16
386bp
14 16
270bp
β-actin2

Figure 3

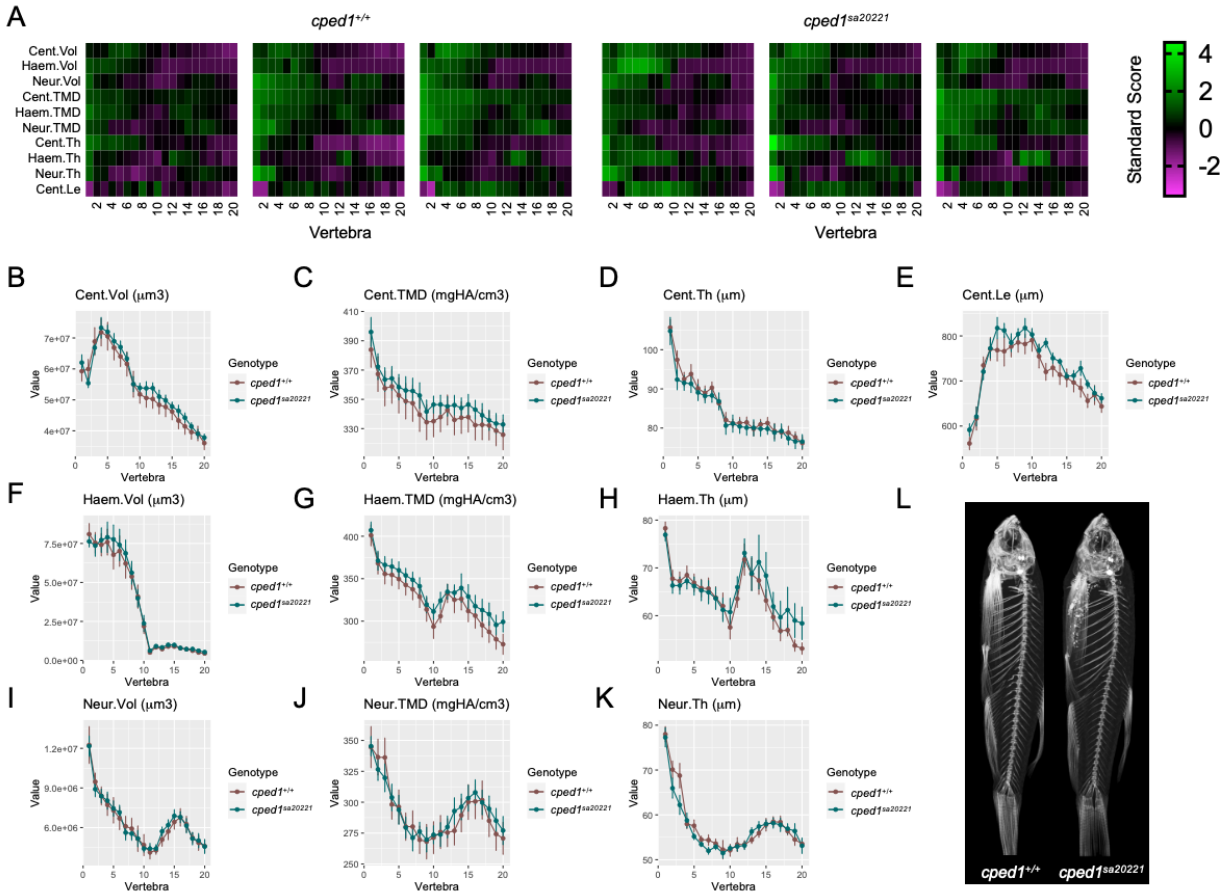
A
cped1+/+
cped1sa20221
Cent.Vol
Haem.Vol
Neur.Vol
Cent.TMD
Haem.TMD
Neur.TMD
Cent.Th
Haem.Th
Neur.Th
Cent.Le
Vertebra
Standard Score
4
2
0
-2
B
Cent.Vol (μm3)
C
Cent.TMD (mgHA/cm3)
D
Cent.Th (μm)
E
Cent.Le (μm)
F
Haem.Vol (μm3)
G
Haem.TMD (mgHA/cm3)
H
Haem.Th (μm)
I
Neur.Vol (μm3)
J
Neur.TMD (mgHA/cm3)
K
Neur.Th (μm)
Value
Genotype
L
cped1+/+
cped1sa20221

Figure 4

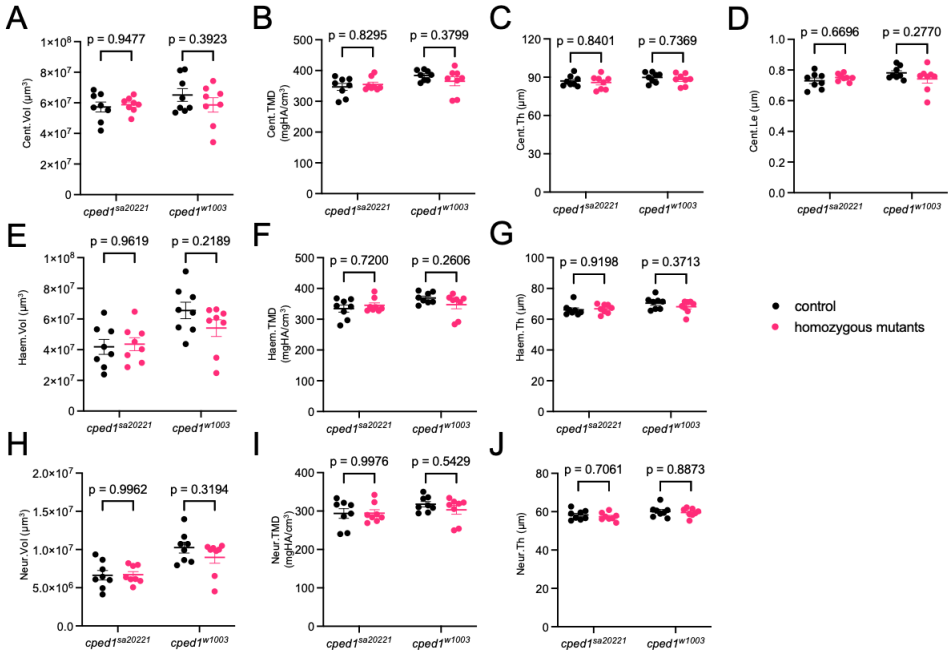
A
p = 0.9477
p = 0.3923
Cent.Vol (µm³)
B
p = 0.8295
p = 0.3799
Cent.TMD (mgHA/cm³)
C
p = 0.8401
p = 0.7369
Cent.Th (µm)
D
p = 0.6696
p = 0.2770
Cent.Le (µm)
E
p = 0.9619
p = 0.2189
Haem.Vol (µm³)
F
p = 0.7200
p = 0.2606
Haem.TMD (mgHA/cm³)
G
p = 0.9198
p = 0.3713
Haem.Th (µm)
H
p = 0.9962
p = 0.3194
Neur.Vol (µm³)
I
p = 0.9976
p = 0.5429
Neur.TMD (mgHA/cm³)
J
p = 0.7061
p = 0.8873
Neur.Th (µm)
cped1sa20221
cped1w1003
control
homozygous mutants

Figure 5

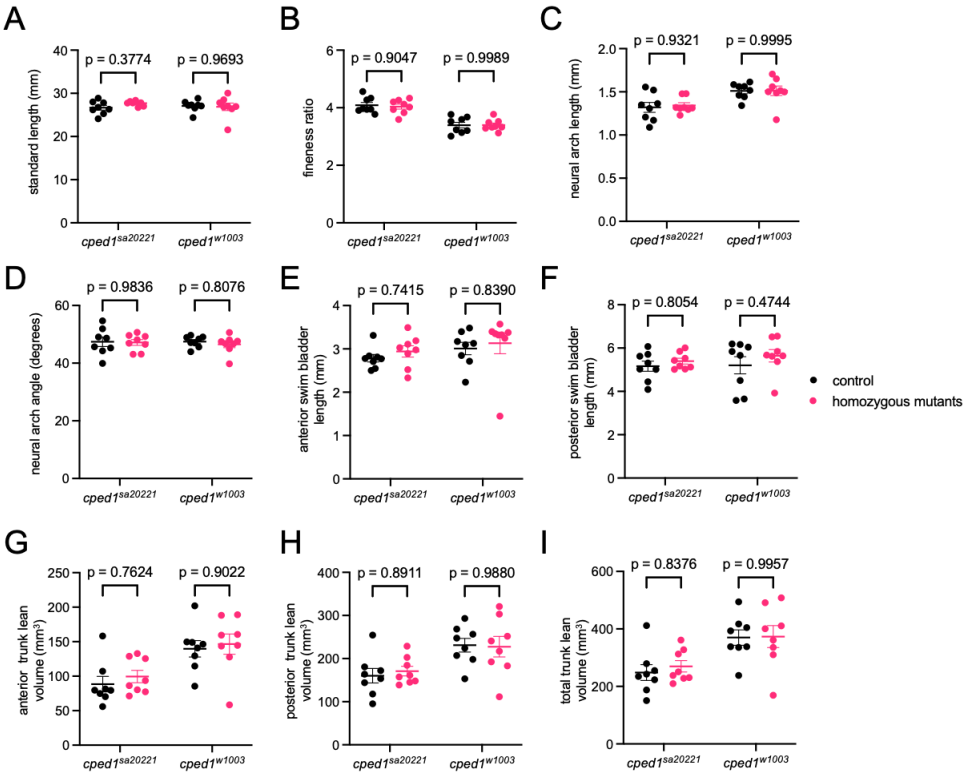
A
standard length (mm)
p = 0.3774
p = 0.9693
B
fineness ratio
p = 0.9047
p = 0.9989
C
neural arch length (mm)
p = 0.9321
p = 0.9995
D
neural arch angle (degrees)
p = 0.9836
p = 0.8076
E
anterior swim bladder length (mm)
p = 0.7415
p = 0.8390
F
posterior swim bladder length (mm)
p = 0.8054
p = 0.4744
control
homozygous mutants
G
anterior trunk lean volume (mm³)
p = 0.7624
p = 0.9022
H
posterior trunk lean volume (mm³)
p = 0.8911
p = 0.9880
I
total trunk lean volume (mm³)
p = 0.8376
p = 0.9957
cped1sa20221
cped1w1003

Figure 6

A

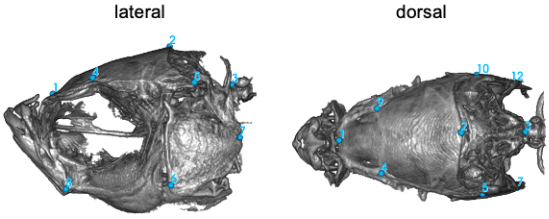

B

Landmarks	Measurement
1-2	frontal bone length
1-3	skull length
4-9	epiphyseal bar length
5-10	dorsal skull width
6-11	ventral skull width
7-12	midline skull width
8-13	distance between anguloarticulars

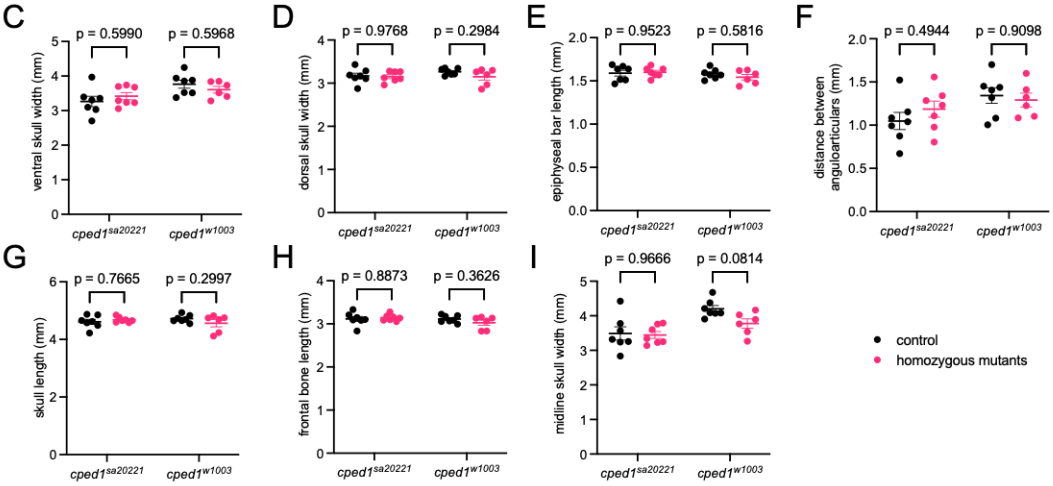

Figure 7

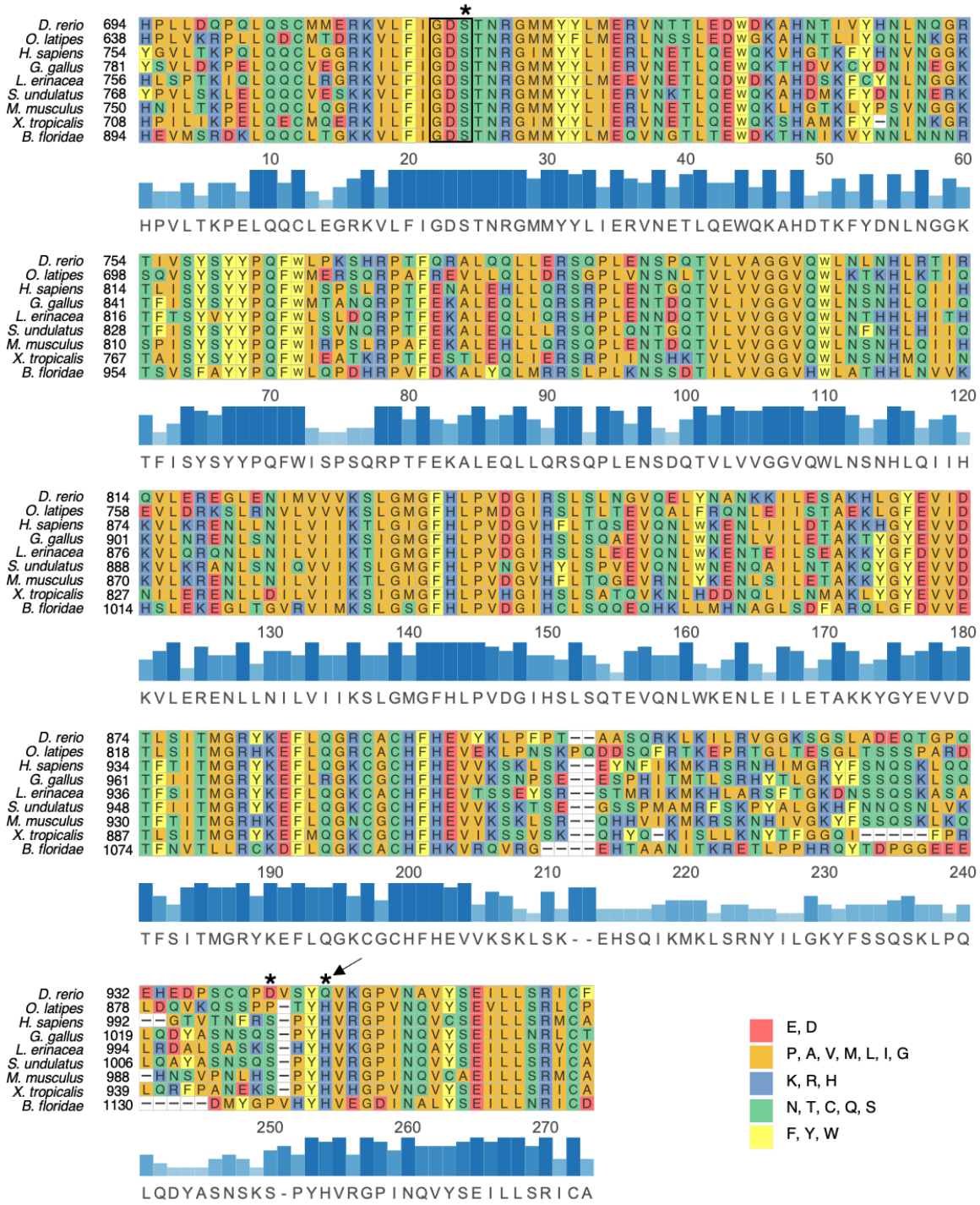
D. rerio
O. latipes
H. sapiens
G. gallus
L. erinacea
S. undulatus
M. musculus
X. tropicalis
B. floridae
HPVLTKPELQQCLEGRKVLFIGDSTNRGMMYYLIERVNETLQEWQKAHDTKFYDNLNGGK
TFISYSYYPQFWISPSQRPTFEKALEQLLQRSQPLENSDQTVLVVGGVQWLNSNHLQIIH
KVLERENLLNILVIIKSLGMGFHLPVDGIHSLSQTEVQNLWKENLEILETAKKYGYEVVD
TFSITMGRYKEFLQGKCGCHFHEVVKSKLSK--EHSQIKMKLSRNYILGKYFSSQSKLPQ
LQDYASNSKS-PYHVRGPINQVYSEILLSRICA
E, D
P, A, V, M, L, I, G
K, R, H
N, T, C, Q, S
F, Y, W